INL/JOU-21-62057-Revision-0

Bulk and surface diffusion of neodymium in alpha-uranium: Ab initio calculations and kinetic Monte Carlo simulations

December 2021

Chao Jiang, Larry K Aagesen Jr, David Andersson, Christopher Matthews, Fergany Badry

Changing the World's Energy Future

INL is a U.S. Department of Energy National Laboratory operated by Battelle Energy Alliance, LLC

INL/JOU-21-62057-Revision-0

Bulk and surface diffusion of neodymium in alpha-uranium: Ab initio calculations and kinetic Monte Carlo simulations

Chao Jiang, Larry K Aagesen Jr, David Andersson, Christopher Matthews, Fergany Badry

December 2021

Idaho National Laboratory
Idaho Falls, Idaho 83415

http://www.inl.gov

Prepared for the
U.S. Department of Energy
Under DOE Idaho Operations Office
Contract DE-AC07-05ID14517

Bulk and surface diffusion of neodymium in alpha-uranium: Ab initio calculations and kinetic Monte Carlo simulations

Chao Jiang,[a,*] Larry K. Aagesen,[a] David Andersson,[b] Christopher Matthews[b] and Fergany Badry[c]

[a]Computational Mechanics and Materials Department, Idaho National Laboratory, Idaho Falls, ID 83415, USA
[b]MST-8, Los Alamos National Laboratory, Los Alamos, NM 87545, USA
[c]Nuclear Engineering Department, Texas A&M University, College Station, TX 77843, USA

Abstract

A fundamental understanding of lanthanide transport in metallic fuels is critical for high fidelity modeling of the fuel-cladding chemical interaction (FCCI) phenomenon, which can lead to the formation of brittle intermetallic compounds and premature failure of the cladding. Here we report a combined ab initio density functional theory (DFT) and kinetic Monte Carlo (KMC) study of the bulk diffusivity of Nd in α-U, fully taking into account the effect of radiation enhanced diffusion. The vacancy mechanism is considered to be the dominant mechanism for the bulk diffusion of Nd since a Nd interstitial is found to be intrinsically unstable in α-U. The surface diffusivity of a Nd adatom on α-U (001) surface has been further predicted using KMC simulations parameterized by DFT calculations. The present study suggests that Nd transport via the surface diffusion mechanism can be many orders of magnitude faster than bulk diffusion. Furthermore, the results from the present lower length scale study can be used to inform mesoscale phase-field simulations to determine the effective diffusion coefficient of Nd through α-U with a porous microstructure.

Keywords: Lanthanide; Fuel-cladding chemical interaction; Diffusion; Kinetic Monte Carlo

*Corresponding author: chao.jiang@inl.gov

1. Introduction

Under irradiation, nuclear fuel may undergo swelling and make contact with the fuel cladding, resulting in the development of an inter-diffusion zone at the fuel/cladding interface. This critical phenomenon, which is called fuel-cladding chemical interaction (FCCI), can lead to breaching and premature failure of the cladding, and is one of the major factors limiting the lifetime and reliability of a fuel design [1]. FCCI is a more severe issue for metallic fuels since they swell much more than oxide fuels, resulting in direct contact of cladding with fuel and fission products at elevated temperature and moderate pressure. For the case of U-Zr metallic fuel and HT-9 stainless steel cladding, the infiltration of lanthanide fission products such as Nd into the cladding will result in the formation of a brittle 'wastage' zone [2], and consequent reduction of cladding strength. These lanthanides are generated inside the fuel pins during the fission of U atoms, with Nd being the most abundant one in irradiated fuel [1].

To date, the dominant mechanism by which lanthanide fission products are transported through the fuel interior towards the fuel/cladding interface is still not fully understood. It has been proposed that the transport of lanthanides through metallic fuels can be greatly accelerated by two "liquid-like" mechanisms [1, 3]. First, lanthanides can rapidly migrate on the internal surfaces of fuel pores, which form under irradiation due to the nucleation and growth of fission gas bubbles. In α-U with an orthorhombic crystal structure, fuel pores may also form due to anisotropic swelling and consequent grain boundary tearing. Diffusion of Xe and Kr fission gases into the grain-boundary voids further transform them into gas bubbles. Importantly, as the fission gas bubbles grow, they eventually become interconnected with each other, creating short-

circuit surface pathways for the transport of fission gas atoms and lanthanides towards the fuel surface. Furthermore, lanthanides may diffuse to the fuel surface through pores filled with liquid Na/Cs, and such a liquid diffusion mechanism has been recently investigated by Li et al. [4, 5] using ab initio molecular dynamics (AIMD) simulations.

For high fidelity modeling of FCCI using the nuclear fuel performance code BISON [6], knowledge of the effective diffusivity of lanthanide fission products through α-U fuel is critically needed. To this end, we have employed in this study a combination of ab initio density functional theory (DFT) calculations and kinetic Monte Carlo (KMC) simulations to predict the bulk diffusivity of Nd through α-U, fully taking into account the effect of radiation enhanced diffusion. We have further considered the migration of Nd adatoms on the α-U (001) surface, which is the most stable (i.e., having the lowest surface energy) among seven low index surfaces considered by Huang and Ju [7]. Importantly, the temperature-dependent bulk and surface diffusivities of Nd in α-U calculated here using lower length scale simulations, together with the diffusion coefficients of Nd in liquid Na/Cs from Li et al. [4, 5], can be used to parameterize mesoscale phase-field simulations using the MARMOT code [8] to determine the effective diffusivity of Nd through α-U fuel with a porous microstructure. The results from phase-field simulations can in turn be used to inform the FCCI model in BISON [6] to more accurately calculate the growth rate of the FCCI layer within the fuel cladding based on the flux of lanthanide fission products from the fuel.

2. Computational methods

2.1. Bulk calculations

Ab initio calculations are performed using projector augmented wave (PAW) pseudopotentials and generalized gradient approximation of Perdew-Burke-Ernzerhof (PBE) [9], as implemented in Vienna ab initio simulation package (VASP) [10]. A large plane-wave cutoff energy of 400 eV and dense Monkhorst-Pack *k*-point meshes are used to ensure high numerical accuracy. Non-spin-polarized calculations are performed for α-U. All calculations include scalar relativistic corrections (i.e., no spin-orbit coupling). Our PBE calculations give unit cell-internal and external parameters of α-U (a_0=2.793 Å, b_0=5.849 Å, c_0=4.896 Å, y=0.098) in good agreement with previous theoretical [7, 11-15] and experimental [16] studies. In particular, our scalar relativistic results are in excellent agreement with those predicted by spin-orbit coupling calculations (a_0=2.797 Å, b_0=5.867 Å, c_0=4.893 Å, y=0.098) [12]. For calculations of point defect energetics, we have employed large 180-atom supercells to minimize artificial defect-defect self-interactions across periodic boundaries, which can be constructed via a 5×3×3 extension of the conventional orthorhombic α-U (space group Cmcm) unit cell. All supercells are fully relaxed with respect to cell-internal atomic positions with the cell volume and shape held fixed, until the Hellmann-Feynman forces are less than 0.02 eV $Å^{-1}$. The conjugate gradient method is used for structural relaxations.

We calculate the formation energies of a vacancy, a self-interstitial atom (SIA), a Nd substitutional (Nd_{sub}), and an interstitial Nd atom (Nd_{int}) in α-U as follows:

$$E_f^{Va} = E(\mathrm{U}_{N-1}) - \frac{N-1}{N} E(\mathrm{U}_N) \quad (1)$$

$$E_f^{SIA} = E(\mathrm{U}_{N+1}) - \frac{N+1}{N} E(\mathrm{U}_N) \quad (2)$$

$$E_f^{Nd_{sub}} = E(\mathrm{U}_{N-1}\mathrm{Nd}_1) - \frac{N-1}{N}E(\mathrm{U}_N) - E(\mathrm{Nd}) \quad (3)$$

$$E_f^{Nd_{int}} = E(\mathrm{U}_N\mathrm{Nd}_1) - E(\mathrm{U}_N) - E(\mathrm{Nd}) \quad (4)$$

where $E(\mathrm{U}_N)$ is the total energy of a perfect α-U supercell containing N lattice sites. $E(\mathrm{U}_{N-1})$, $E(\mathrm{U}_{N+1})$, $E(\mathrm{U}_{N-1}\mathrm{Nd}_1)$, and $E(\mathrm{U}_N\mathrm{Nd}_1)$ are the total energies of α-U supercells containing one vacancy, one SIA, one Nd substitutional, and one Nd interstitial, respectively. $E(\mathrm{Nd})$ is the total energy (normalized per atom) of pure Nd in its ground-state dhcp (space group $P6_3/mmc$) structure.

The binding energy between a Nd substitutional and a vacancy or SIA can be further calculated as follows:

$$E_{Bind}^{Nd_{sub}-Va} = E(\mathrm{U}_{N-1}\mathrm{Nd}_1) + E(\mathrm{U}_{N-1}) - E(\mathrm{U}_N) - E(\mathrm{U}_{N-2}\mathrm{Nd}_1) \quad (5)$$

$$E_{Bind}^{Nd_{sub}-SIA} = E(\mathrm{U}_{N-1}\mathrm{Nd}_1) + E(\mathrm{U}_{N+1}) - E(\mathrm{U}_N) - E(\mathrm{U}_N\mathrm{Nd}_1) \quad (6)$$

where $E(\mathrm{U}_{N-2}\mathrm{Nd}_1)$ is the total energy of α-U supercell containing one Nd_{sub}-vacancy pair. Here a positive binding energy indicates attraction between the two defects, and vice versa.

3.2. Diffusion of Nd in α-U via the vacancy mechanism

From our CI-NEB calculations using 180-atom supercells and 3 intermediate images, we obtain the activation energy for the rate-limiting step along this path (configuration 1 → 3) to be 1.358 eV (see Fig. 4h). For the reverse transformation of configuration 2 → 1, the activation barrier for its rate-limiting step (configuration 2 → 3) is calculated to be 1.126 eV. Fig. 5

illustrates another possible diffusion mechanism for Nd migration in α-U, in which Nd migrates by exchanging position with a nearby vacancy along the *c* axis with a low barrier of only 0.180 eV. Finally, we have considered the diffusion of a Nd_{sub}-vacancy pair perpendicular to the corrugated (010) plane via the configuration $1 \rightarrow 6 \rightarrow 6 \rightarrow 1$ path shown in Fig. 6. The rate-limiting step along this path is the transformation of configuration $1 \rightarrow 6$ with a barrier of 2.555 eV, which is significantly higher than those for Nd diffusion within the corrugated (010) plane.

To compute the diffusivity of Nd within the (010) plane of α-U, we have performed KMC simulations implementing a rejection-free residence time algorithm [20]. For a Nd_{sub}-vacancy pair in configuration 1, two types of diffusion events have been considered: (i) the transformation of configuration $1 \rightarrow 3$ as depicted in Fig. 4, and (ii) vacancy-Nd exchange hop as illustrated in Fig. 5. A Nd_{sub}-vacancy pair in configuration 2 is only allowed to transform into configuration 3. Finally, a Nd_{sub}-vacancy pair in configuration 3 can transform to either configuration 1 or configuration 2. In view of the large Nd_{sub}-vacancy binding energy, it is assumed that vacancy jumps that lead to the complete dissociation of a Nd_{sub}-vacancy pair are rare events. Such jumps are therefore not included in the present KMC simulations.

According to transition state theory, the hopping rate between different Nd_{sub}-vacancy pair configurations can be calculated using the Arrhenius equation:

$$\Gamma = \nu_0 e^{-\frac{E_{mig}}{k_B T}} \tag{7}$$

where E_{mig} is the migration barrier for a given diffusion pathway from NEB calculations, k_B is the Boltzmann constant, and ν_0 is the attempt frequency that can be calculated from the real

vibrational frequencies of the initial state and the transition state. Instead of computing all $3N$ vibrational modes in a N-atom α-U supercell, which is computationally demanding when N is large, we have considered only the vibrational modes of the migrating atoms, with all other atoms held fixed [21]. Our final calculated attempt frequencies and migration barriers are summarized in Table 3.

For good statistical accuracy, 1000 non-interacting Nd_{sub}-vacancy pairs are used in our KMC simulations to generate the mean squared displacement (MSD) data for Nd atoms, decomposed along the *a* and *c* directions, respectively. Initially, all 1000 Nd_{sub}-vacancy pairs are in configuration 1. They can either transform into configuration 2 via configuration 3 as an intermediate state or remain in configuration 1 after many vacancy-Nd exchange hops. At each KMC step, a random number is generated to pick one jump from a list of all possible jump events, with the average residence time given by the reciprocal of the sum of all rates. After the chosen jump is performed, the new position of the Nd atom within the Nd_{sub}-vacancy pair is calculated. Note that, by considering only the interconversions between configurations 1 and 2, diffusion of Nd is constrained to be within the (010) plane in our KMC simulations. Finally, the anisotropic diffusivities of Nd along *a* and *c* directions in α-U can be determined through a least-square fitting of MSD vs time data using the Einstein relation for one-dimensional motion, $\mathrm{MSD} = 2Dt$.

The diffusivity of Nd along the *b* axis, which is not considered in our KMC simulations, can be estimated using the following equation:

$$D_{Nd}^{b} = f\nu_0 \left(\frac{b_0}{2}\right)^2 e^{-\frac{E_{mig}}{k_B T}} \quad (8)$$

where f is the correlation factor that accounts for the deviation from random walk behavior, and is assumed to be 1 in the present work. b_0=5.849 Å is the equilibrium lattice constant of α-U. The attempt frequency ν_0 is assumed to be equal to the value for the vacancy-Nd exchange hop (see Table 3). E_{mig}=2.555 eV is the migration barrier from CI-NEB calculations (Fig. 6). Our final calculated Nd diffusivities in bulk α-U are shown in Fig. 7. Due to the orthorhombic symmetry of α-U, Nd diffuses anisotropically along *a*, *b*, and *c* directions. It can be seen that Nd diffusion along the *b* axis is significantly slower than the other two directions. Note that taking into account the correlation effects will further reduce D_{Nd}^{b}. The calculation of the correlation factor f in a low-symmetry crystal such as α-U can nevertheless be quite involved and is beyond the scope of this study. The diffusivity of Nd along the *a* axis also differs from that along the *c* axis, with the former being slightly higher than the latter. By averaging over the anisotropic Nd diffusivities along all three directions, we have calculated the isotropic Nd diffusivity in a polycrystalline α-U microstructure as:

$$D_{Nd}^{bulk} = \frac{D_{Nd}^{a}+D_{Nd}^{b}+D_{Nd}^{c}}{3} \approx \frac{D_{Nd}^{a}+D_{Nd}^{c}}{3} \quad (9)$$

As shown in Fig. 7, the calculated average (isotropic) diffusivity (in m^2/s) of Nd in α-U over a wide temperature range can be accurately fitted using the following Arrhenius equation:

$$D_{Nd}^{bulk} = 4.007 \times 10^{-8} \mathrm{e}^{-\frac{16344.46}{T}} \quad (10)$$

It is worth noting that, one implicit assumption in our KMC simulations is that there exist abundant irradiation-induced vacancies in α-U to assist the migration of substitutional Nd atoms. In general, this is not the case, and the true Nd diffusivity should be calculated by multiplying Eq. (10) by the probability of finding a vacancy in the first nearest neighbor shell of a substitutional Nd atom. Such a probability can be calculated as follows:

$$p = c_v \sum_s e^{\frac{E_{Bind}^s}{k_B T}} \tag{11}$$

where c_v is the free vacancy concentration in the α-U matrix. The summation goes through all lattice sites s that are nearest neighbors of Nd. E_{Bind}^s is the binding energy between Nd and a vacancy occupying site s, which can be found in Table 2. For large positive values of E_{Bind}^s, the probability p will be significantly enhanced compared to the free vacancy concentration c_v, which is the case for Nd in α-U. The true Nd diffusivity will be calculated in the following Section.

3.3. Effects of irradiation on Nd diffusion

Under irradiation, point defects can be generated in amounts far beyond their equilibrium concentrations, leading to radiation enhanced diffusion. For the simple case of a pure α-U metal, the non-equilibrium concentrations of vacancies (c_v) and self-interstitials (c_i) can be estimated using rate theory [22] by solving the following two equations:

$$\frac{\partial c_v}{\partial t} = \zeta\phi - R_{iv} c_i c_v - K_{tot}^2 D_v (c_v - c_v^{th}) \tag{12}$$

$$\frac{\partial c_i}{\partial t} = \zeta\phi - R_{iv} c_i c_v - K_{tot}^2 D_i c_i \tag{13}$$

where ϕ is the dose rate in displacement per atom per second (dpa/s). ζ is the defect production efficiency, or the fraction of point defects surviving in-cascade recombination [23]. D_v and D_i denote vacancy and interstitial diffusivities, respectively. K_{tot}^2 is the total sink strength for mobile point defects due to e.g. dislocations and grain boundaries. The sink strength for vacancies and interstitials are treated as equal. The concentration of interstitials in thermal equilibrium is assumed to be zero. c_v^{th} is the thermal equilibrium vacancy concentration in α-U and can be calculated as:

$$c_v^{th} = e^{S_f^{Va}} e^{-\frac{E_f^{Va}}{k_B T}} \tag{14}$$

where E_f^{Va} is the vacancy formation energy in α-U; its value can be found in Table 1. To obtain the vacancy formation entropy, S_f^{Va}, phonon calculations will need to be performed for both perfect and defective α-U supercells. Due to the high computational cost of such calculations, a typical value for metals, i.e., $S_f^{Va} = 2.0\ k_B$ [24], is adopted in the present study.

In Eqs. (12) and (13), R_{iv} is the rate constant for vacancy-interstitial mutual recombination and can be calculated as:

$$R_{iv} = \frac{4\pi r_c}{V_a}(D_i + D_v) \tag{15}$$

where r_c represents the instantaneous recombination radius between interstitials and vacancies. $V_a = a_0 b_0 c_0/4$ is the atomic volume.

The steady state is reached when $\frac{\partial c_v}{\partial t} = 0$ and $\frac{\partial c_i}{\partial t} = 0$, which gives the vacancy concentration under irradiation as:

$$c_v = -\frac{D_i K_{tot}^2}{2R_{iv}} + \frac{c_v^{th}}{2} + \sqrt{\left(\frac{D_i K_{tot}^2}{2R_{iv}} + \frac{c_v^{th}}{2}\right)^2 + \frac{D_i \zeta \phi}{D_v R_{iv}}} \tag{16}$$

Using the direction-dependent vacancy and SIA migration barriers in α-U calculated by Huang and Wirth [13], we have calculated the anisotropic diffusivities for vacancy and SIA along *a*, *b*, and *c* directions as:

$$D_{v/i}^a = \nu_0 a_0^2 e^{-\frac{E_{mig}^{[100]}}{k_B T}} \tag{17}$$

$$D_{v/i}^b = \nu_0 \left(\frac{b_0}{2}\right)^2 e^{-\frac{E_{mig}^{[010]}}{k_B T}} \tag{18}$$

$$D_{v/i}^c = \nu_0 \left(\frac{c_0}{2}\right)^2 e^{-\frac{E_{mig}^{[001]}}{k_B T}} \tag{19}$$

where $E_{mig}^{[hkl]}$ represents the migration barrier for a vacancy or a SIA along the [*hkl*] direction. ν_0 is assumed to be equal to the Einstein frequency of α-U, which is 2.88 THz according to the vibrational frequency calculations by Taylor [12]. The average vacancy and SIA diffusivities in α-U can then be obtained as:

$$D_{v/i} = \frac{D_{v/i}^a + D_{v/i}^b + D_{v/i}^c}{3} \tag{20}$$

Figs. 8a and 8b show our calculated steady-state vacancy concentration and bulk diffusivity of Nd in α-U under irradiation, respectively. A dose rate of 10^{-6} dpa/s and a defect production efficiency of ~0.3, which was predicted by molecular dynamics simulations for high-energy cascades in bcc Fe [23], are assumed in our calculations. A total sink strength of 10^{13} m^{-2} is further assumed for vacancies and SIAs. The capture radius r_c for the mutual recombination of a vacancy with a SIA is estimated to be 7.82 Å such that the recombination volume $\frac{4}{3}\pi r_c^3$ is equal to $100V_a$ [25]. Importantly, significant radiation-enhanced diffusion of Nd is predicted by the present calculations at low temperatures, which is due to a supersaturation of vacancies created by collision cascades. At high temperatures, however, the radiation effects become negligible as the Nd diffusivities under irradiation and equilibrium conditions become identical. It can also be seen that KMC simulations assuming that all Nd atoms are bound by vacancies will significantly overestimate the bulk diffusivity of Nd in α-U.

3.3. Migration of Nd adatom on α-U (001) surface

Among all possible adsorption sites (hollow1, hollow2, atop, bridge) on the α-U (001) surface, our DFT calculations find the hollow1 site to be the energetically most favorable for Nd adatoms (Table 4). Figs. 9 and 10 illustrate the hopping of a Nd adatom from one hollow1 site to a neighboring one along the [100] and [110] directions, respectively. The calculated attempt frequencies and migration barriers for the two paths are reported in Table 5. Fig. 11a further shows our KMC calculated anisotropic diffusivities of Nd adatom along *a* and *b* axis on α-U (001) surface. Diffusion of a Nd adatom is significantly faster along the *a* axis than along the *b*

axis. As shown in Fig. 11b, the average surface diffusivity (in m^2/s) of Nd on the α-U (001) surface over a wide temperature range can be well described by the following Arrhenius equation:

$$D_{Nd}^{surface} = 5.916 \times 10^{-8} \mathrm{e}^{-\frac{919.47}{T}} \quad (21)$$

In Fig. 11b, our calculated bulk diffusivities of Nd in α-U as well as the Nd diffusivity in liquid Na from Li et al. [4] are also shown for comparison. It can be seen that Nd transport via either surface diffusion or liquid diffusion mechanisms is many orders of magnitude faster than bulk diffusion even after the radiation-enhanced diffusion effect has been taken into account.

4. Conclusions

In this study, the temperature-dependent bulk and surface diffusivities of Nd in α-U have been rigorously calculated from lower length scale simulations integrating ab initio density functional theory calculations and kinetic Monte Carlo simulations. Our key findings are summarized as follows:

(i) Since a Nd interstitial is unstable in α-U and will spontaneously transform into a Nd substitutional and a U-SIA, fast migration of Nd via the interstitial mechanism should be ruled out. The vacancy mechanism will be the dominant mechanism for bulk diffusion of Nd in α-U under irradiation.

(ii) Repeated interconversions between different configurations of a Nd_{sub}-vacancy pair can lead to the long-range migration of Nd within the corrugated (010) plane of α-U. Nd diffusion perpendicular to the (010) plane, however, is many orders of magnitude slower.

(iii) At low temperatures, the bulk diffusivity of Nd in α-U can be significantly accelerated by radiation due to the presence of supersaturated vacancies, although such an enhancement will be negligible at high temperatures.

(iv) Diffusion of Nd adatoms via interconnected pore surfaces in α-U can be many orders of magnitude faster than bulk diffusion.

For future studies, the incorporation of the effects of solute-vacancy trapping [26, 27] on defect evolution in rate theory model will be of great interest. To consider such effects, two terms describing the trapping of freely migrating vacancies by Nd substitutionals and the dissociation of vacancies from Nd_{sub}-vacancy pairs, respectively, need to be incorporated into Eq. (12). A term representing the recombination of Nd_{sub}-vacancy pairs with SIAs to form Nd substitutionals should also be included in Eq. (13). Presumably, by explicitly solving the coupled rate equations that describe the time evolutions of the concentrations of vacancies, SIAs, Nd substitutionals not bound to vacancies, and Nd_{sub}-vacancy pairs, more accurate predictions of bulk diffusivities of Nd in α-U can be obtained.

Furthermore, in the present KMC simulations, only Nd_{sub}-vacancy pairs have been considered. In future studies, the possibility that a Nd atom can bind multiple vacancies to form larger Nd_{sub}-vacancy complexes can be further explored. DFT calculations of the most stable configurations and associated migration barriers of such defect complexes will also be of interest.

Conflicts of interest

There are no conflicts to declare.

Acknowledgements

This work was fully sponsored by the U.S. Department of Energy, Office of Nuclear Energy, Nuclear Energy Advanced Modeling and Simulation (NEAMS) Program at Idaho National Laboratory operated by Battelle Energy Alliance (BEA) under DOE-NE Idaho Operations Office Contract DE-AC07-05ID14517. Los Alamos National Laboratory, an affirmative action/equal opportunity employer, is operated by Triad National Security, LLC, for the National Nuclear Security Administration of the U.S. Department of Energy under Contract No. 89233218CNA000001. The authors thank Benjamin Beeler from North Carolina State University for helpful discussions. All DFT calculations are performed using the FALCON supercomputer at Idaho National Laboratory.

References

[1] C. Matthews, C. Unal, J. Galloway, D.D. Keiser Jr., S.L. Hayes, Fuel-cladding chemical interaction in U-Pu-Zr metallic fuels: A critical review, Nucl. Technol. 198 (2017) 231-259.

[2] J.M. Harp, D.L. Porter, B.D. Miller, T.L. Trowbridge, W.J. Carmack, Scanning electron microscopy examination of a Fast Flux Test Facility irradiated U-10Zr fuel cross section clad with HT-9, J. Nucl. Mater. 494 (2017) 227-239.

[3] R.D. Mariani, D.L. Porter, T.P. O'Holleran, S.L. Hayes, J.R. Kennedy, Lanthanides in metallic nuclear fuels: Their behavior and methods for their control, J. Nucl. Mater. 419 (2011) 263-271.

[4] X. Li, A. Samin, J. Zhang, C. Unal, R.D. Mariani, Ab-initio molecular dynamics study of lanthanides in liquid sodium, J. Nucl. Mater. 484 (2017) 98-102.

[5] X. Li, J. Zhang, C. Unal, R.D. Mariani, Behaviors of Ce, Pr, and Nd in liquid cesium by ab initio molecular dynamics simulations, J. Appl. Phys. 124 (2018) 135102.

[6] R.L. Williamson, J.D. Hales, S.R. Novascone, M.R. Tonks, D.R. Gaston, C.J. Permann, D. Andrs, R.C. Martineau, Multidimensional multiphysics simulation of nuclear fuel behavior, J. Nucl. Mater. 423 (2012) 149-163.

[7] S.Q. Huang, X.H. Ju, First-principles study of properties of alpha uranium crystal and seven alpha uranium surfaces, J. Chem. 2017 (2017) 8618340.

[8] M.R. Tonks, D. Gaston, P.C. Millett, D. Andrs, P. Talbot, An object-oriented finite element framework for multiphysics phase field simulations, Comp. Mat. Sci. 51 (2012) 20-29.

[9] J.P. Perdew, K. Burke, M. Ernzerhof, Generalized gradient approximation made simple, Phys. Rev. Lett. 77 (1996) 3865-3868.

[10] G. Kresse, J. Furthmuller, Efficient iterative schemes for ab initio total-energy calculations using a plane-wave basis set, Phys. Rev. B 54 (1996) 11169-11186.

[11] P. Söderlind, First-principles elastic and structural properties of uranium metal, Phys. Rev. B 66 (2002) 085113.

[12] C.D. Taylor, Evaluation of first-principles techniques for obtaining materials parameters of α-uranium and the (001) α-uranium surface, Phys. Rev. B 77 (2008) 094119.

[13] G.Y. Huang, B.D. Wirth, First-principles study of diffusion of interstitial and vacancy in α U-Zr, J. Phys.: Condens. Matter. 23 (2011) 205402.

[14] B. Beeler, C. Deo, M. Baskes, M. Okuniewski, First principles calculations of the structure and elastic constants of α, β and γ uranium, J. Nucl. Mater. 433 (2013) 143-151.

[15] B. Beeler, B. Good, S. Rashkeev, C. Deo, M. Baskes, M. Okuniewski, First principles calculations for defects in U, J. Phys.: Condens. Matter. 22 (2010) 505703.

[16] C.S. Barrett, M.H. Mueller, R.L. Hitterman, Crystal structure variations in alpha uranium at low temperatures, Phys. Rev. 129 (1963) 625-629.

[17] G. Henkelman, B.P. Uberuaga, H. Jonsson, A climbing image nudged elastic band method for finding saddle points and minimum energy paths, J. Chem. Phys. 113 (2000) 9901-9904.

[18] K.R. Lund, K.G. Lynn, M.H. Weber, C. Macchi, A. Somoza, A. Juan, M.A. Okuniewski, Impurity migration and effects on vacancy formation enthalpy in polycrystalline depleted uranium, J. Nucl. Mater. 466 (2015) 343-350.

[19] J.L. Bocquet, C. Barouh, C.C. Fu, Migration mechanism for oversized solutes in cubic lattices: The case of yttrium in iron, Phys. Rev. B 95 (2017) 214108.

[20] Y. Zhang, C. Jiang, X. Bai, Anisotropic hydrogen diffusion in α-Zr and Zircaloy predicted by accelerated kinetic Monte Carlo simulations, Sci. Rep. 7 (2017) 41033.

[21] H. Wu, T. Mayeshiba, D. Morgan, High-throughput ab-initio dilute solute diffusion database, Sci. Data 3 (2016) 160054.

[22] R. Sizmann, The effect of radiation upon diffusion in metals, J. Nucl. Mater. 69-70 (1978) 386-412.

[23] L. Malerba, Molecular dynamics simulation of displacement cascades in α-Fe: A critical review, J. Nucl. Mater. 351 (2006) 28-38.

[24] J.J. Burton, Vacancy-formation entropy in cubic metals, Phys. Rev. B 5 (1972) 2948-2957.

[25] N.Q. Lam, Radiation-induced defect buildup and radiation-enhanced diffusion in a foil under energetic bombardment, J. Nucl. Mater. 56 (1975) 125-135.

[26] M.J. Hackett, R. Najafabadi, G.S. Was, Modeling solute-vacancy trapping at oversized solutes and its effect on radiation-induced segregation in Fe–Cr–Ni alloys, J. Nucl. Mater. 389 (2009) 279-287.

[27] Y. Katoh, A. Kohyama, The influence of impurity trapping on formation and growth of defect clusters in irradiated materials, Nucl. Instrum. Methods Phys. Res. B 102 (1995) 12-18.

Table 1. DFT calculated point defect formation energies (eV) in α-U in comparison with previous studies. The most stable configuration for SIA is a U atom occupying a pentahedron interstitial site. The ground state configuration of a Nd interstitial is a Nd substitutional with a bound SIA.

Defect type	This work	Previous studies
Vacancy	1.78	1.95 [12] 1.69 [13] 1.86 [15] 1.60 [18]
SIA	4.20	4.42 [13]
Nd substitutional	2.15	
Nd interstitial (pentahedron site)	7.82	
Nd interstitial (tetrahedron site)	7.30	
Nd interstitial (Nd_{sub}+SIA)	6.01	

Table 2. DFT calculated binding energies (eV) between a U vacancy and a Nd substitutional in α-U.

Nd_{sub}-vacancy pair configuration	Binding energy
1	1.25
2	0.95
3	-0.04
4	0.21
5	0.14
6	0.10

Table 3. DFT calculated attempt frequencies (THz) and migration barriers (eV) for Nd jumps in bulk α-U.

Path	Attempt frequency	Migration barrier
Configuration 1 to 3	3.07	1.358
Configuration 3 to 1	3.25	0.071
Configuration 2 to 3	3.68	1.126
Configuration 3 to 2	3.37	0.139
Vacancy-Nd exchange hop (Configuration 1 to 1)	2.90	0.180

Table 4. DFT calculated adsorption energy (eV) of a Nd adatom at different sites on α-U (001) surface. Adsorption energies relative to the hollow1 site are shown.

Surface site	ΔE
Hollow1	0
Hollow2	0.067
Atop	0.245
Bridge	0.430

Table 5. DFT calculated attempt frequencies (THz) and migration barriers (eV) for Nd adatom hopping between adjacent Hollow1 sites on α-U (001) surface.

Path	Attempt frequency	Migration barrier
Along [100] direction	1.10	0.067
Along [110] direction	1.03	0.258

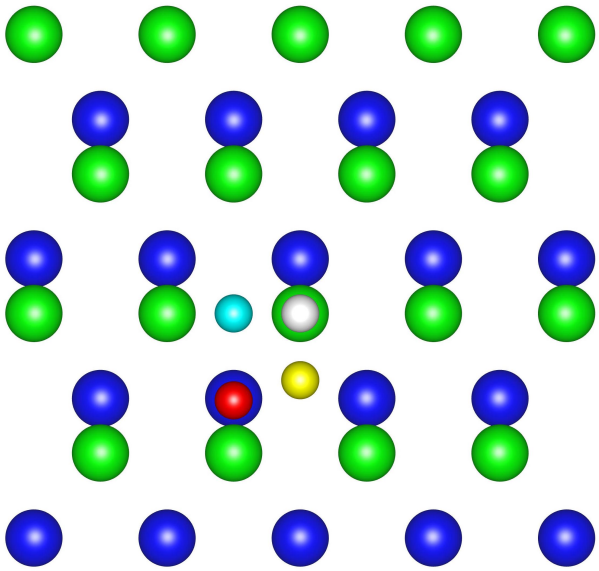

Fig. 1. Possible adsorption sites for Nd adatom on the α-U (001) surface. Top layer and second layer U atoms are shown as green and blue spheres, respectively. Red, yellow, cyan and white spheres represent hollow1, hollow2, bridge and atop sites, respectively.

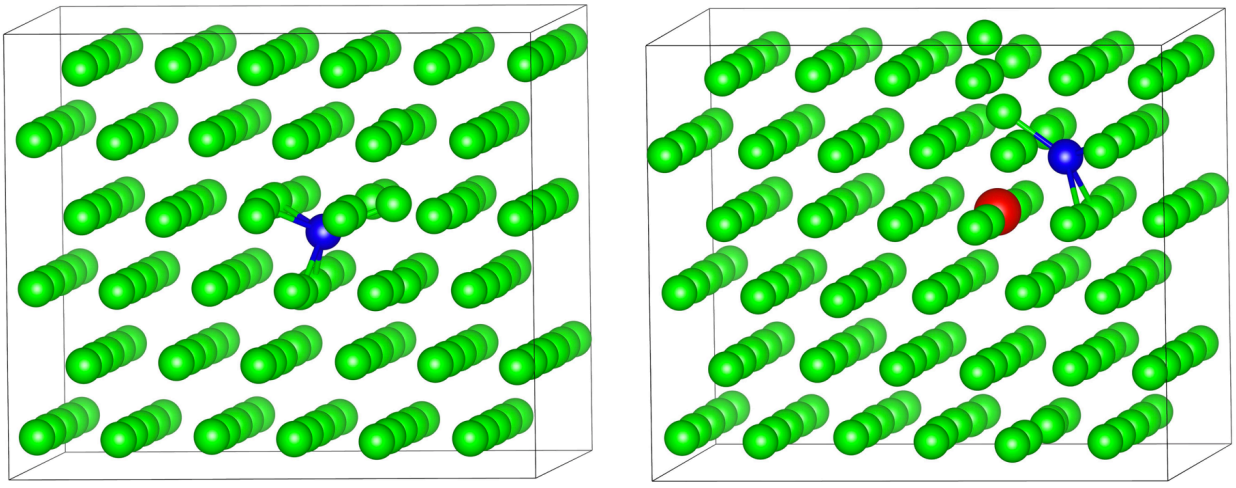

(a) U-SIA (b) Nd interstitial

Fig. 2. Ground-state configurations of (a) U-SIA and (b) Nd interstitial defects in α-U. Green and red spheres represent U and Nd atoms, respectively. Blue sphere represents a U-SIA.

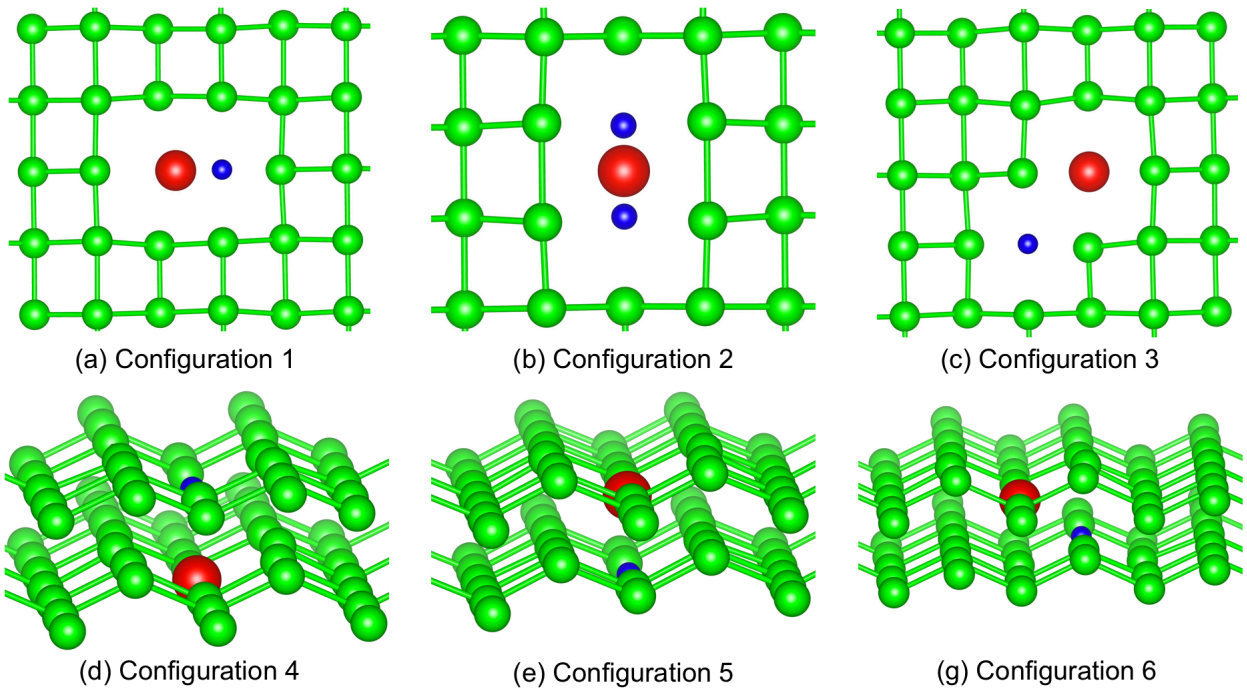

Fig. 3. Different configurations of a Nd_{sub}-vacancy pair in α-U. Green and red spheres represent U and Nd atoms, respectively. Blue spheres represent a half-vacancy in configuration 2 and a vacancy in the other configurations. Nearest neighbor U-U bonds are shown to aid the visualization of Nd_{sub}-vacancy pair structures. In configurations 1, 3, 4, 5, and 6, the Nd_{sub}-vacancy pair is approximately along the [001], [201], [1-10], [110], and [212] directions, respectively. In configuration 2, the two half-vacancies and Nd atom are aligned along the [100] direction.

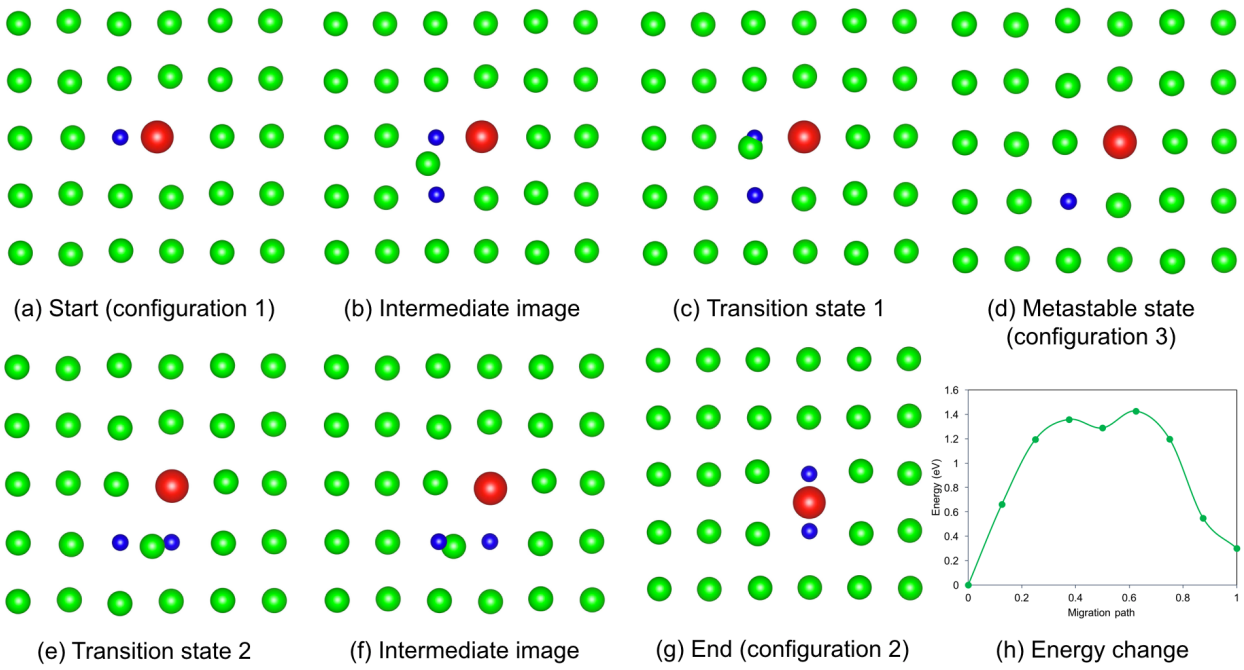

Fig. 4. Vacancy-assisted migration of Nd within the corrugated (010) plane of α-U by interconversion between configurations 1 and 2 for a Nd_{sub}-vacancy pair. Green and red spheres represent U and Nd atoms, respectively. Blue spheres represent a vacancy or a half vacancy. The energy changes along the NEB calculated minimum energy path are shown in (h).

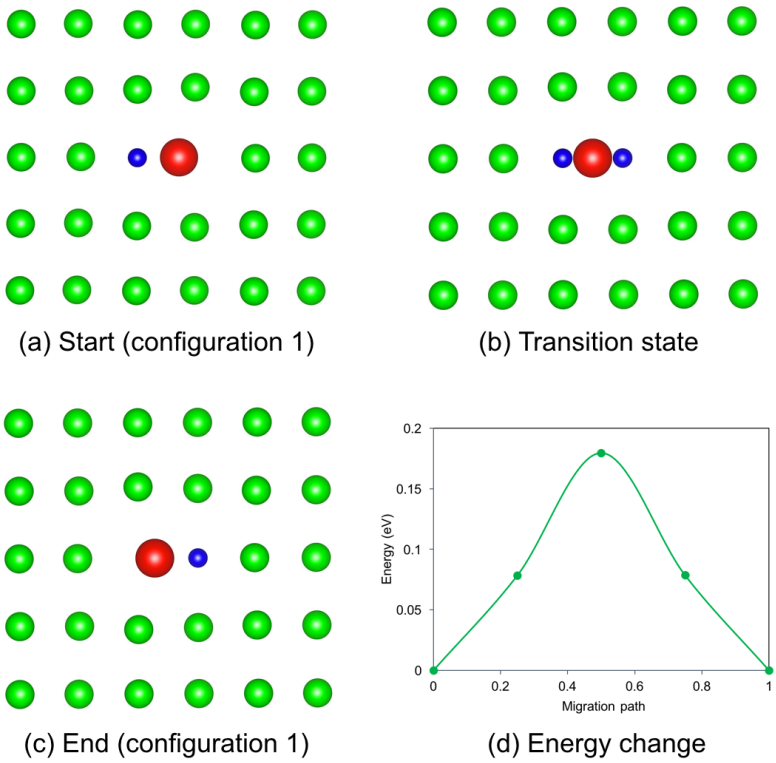

Fig. 5. Nd migration within the (010) plane of α-U by exchanging position with a nearest-neighbor vacancy along the *c* axis. Both the start and end states correspond to configuration 1 of a Nd_{sub}-vacancy pair. Green and red spheres represent U and Nd atoms, respectively. Blue spheres represent a vacancy or a half-vacancy. The energy changes along the NEB calculated minimum energy path are shown in (d).

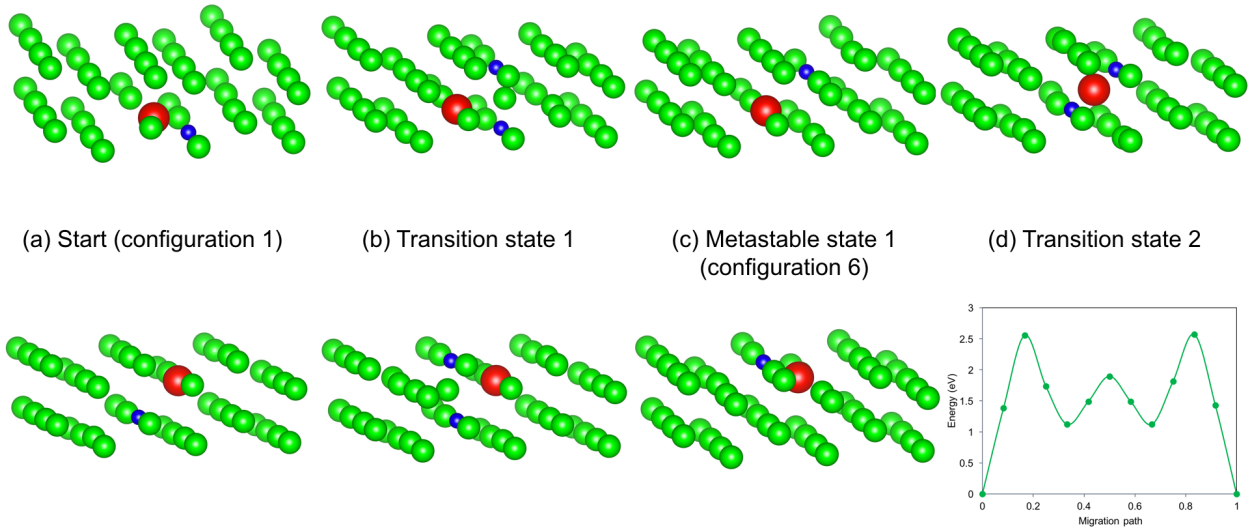

Fig. 6. Vacancy-assisted migration of Nd perpendicular to the (010) plane of α-U. Both the start and end states correspond to a Nd_{sub}-vacancy pair in configuration 1. The two metastable states correspond to a Nd_{sub}-vacancy pair in configuration 6. Green and red spheres represent U and Nd atoms, respectively. Blue sphere represents a U vacancy. The energy changes along the NEB calculated minimum energy path are shown in (h).

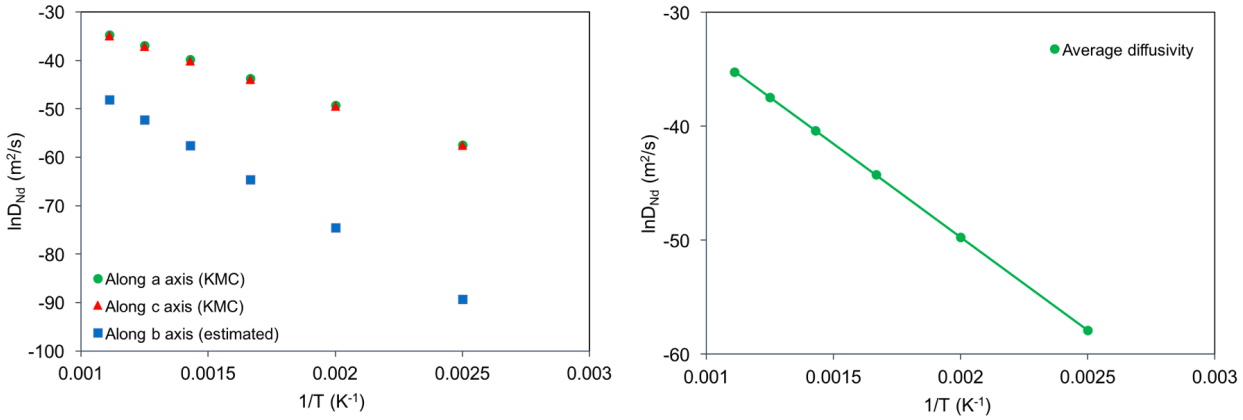

(a) Anisotropic (b) Average

Fig. 7. (a) Arrhenius plot for anisotropic diffusivity of Nd along *a*, *b*, and *c* axis in single-crystal α-U. (b) Arrhenius plot for average (isotropic) diffusivity of Nd in polycrystalline α-U. Nd diffusivities along *a* and *c* directions are obtained from KMC simulations assuming that all Nd atoms form stable Nd_{sub}-vacancy pairs, i.e. p=1. The solid line represents the best fitting of KMC data using the Arrhenius equation.

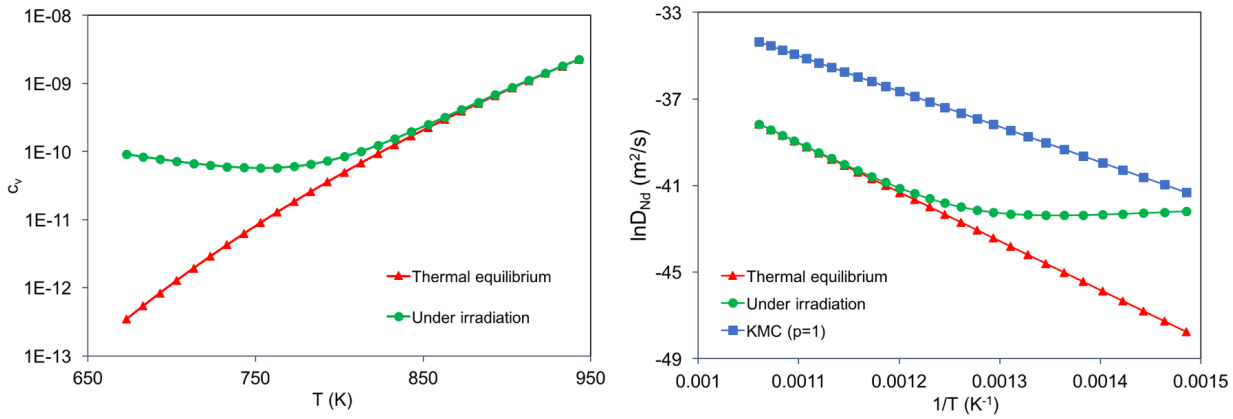

(a) Vacancy concentration (b) Nd diffusivity

Fig. 8. (a) Vacancy concentration in α-U under both thermal equilibrium and irradiation conditions, plotted as a function of temperature. (b) Arrhenius plot for average diffusivity of Nd in α-U under both equilibrium and irradiation conditions. Results from KMC simulations assuming that all Nd atoms are bound by vacancies are also shown for comparison.

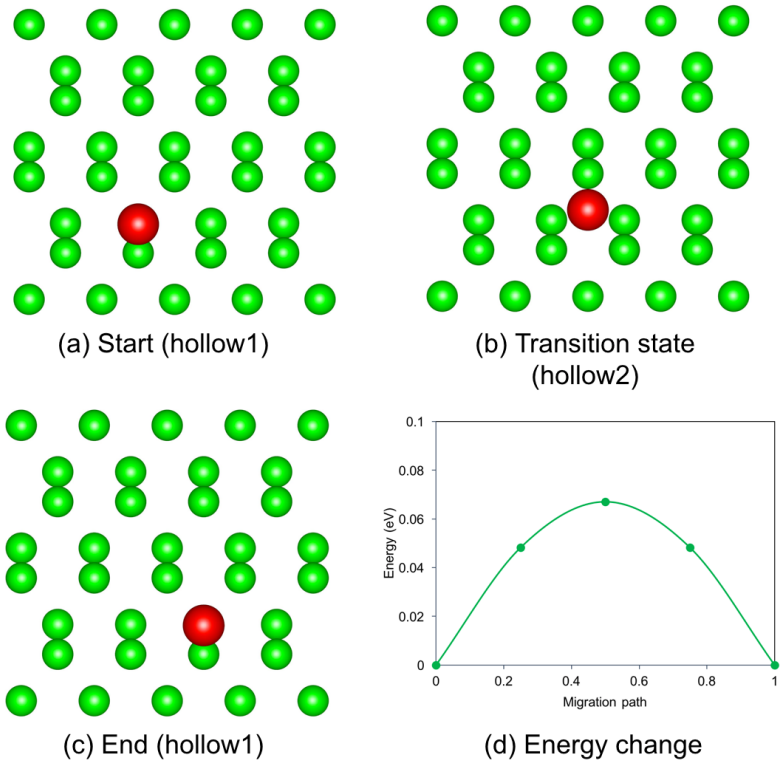

Fig. 9. Direct hollow1 → hollow1 jump of a Nd adatom along the [100] direction on the α-U (001) surface, with the hollow2 site being the transition state. Green and red spheres represent U and Nd atoms, respectively. The energy changes along the NEB calculated minimum energy path are shown in (d).

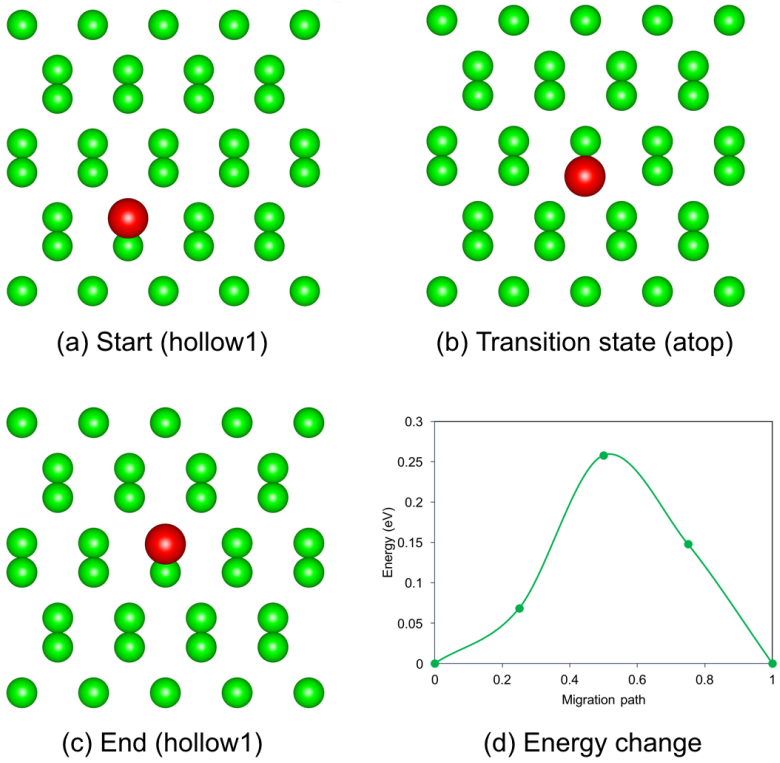

Fig. 10. Nd adatom hopping on the (001) surface of α-U along the [110] direction via the hollow1 → hollow1 path, with the atop site being the transition state. Green and red spheres represent U and Nd atoms, respectively. The energy changes along the NEB calculated minimum energy path are shown in (d).

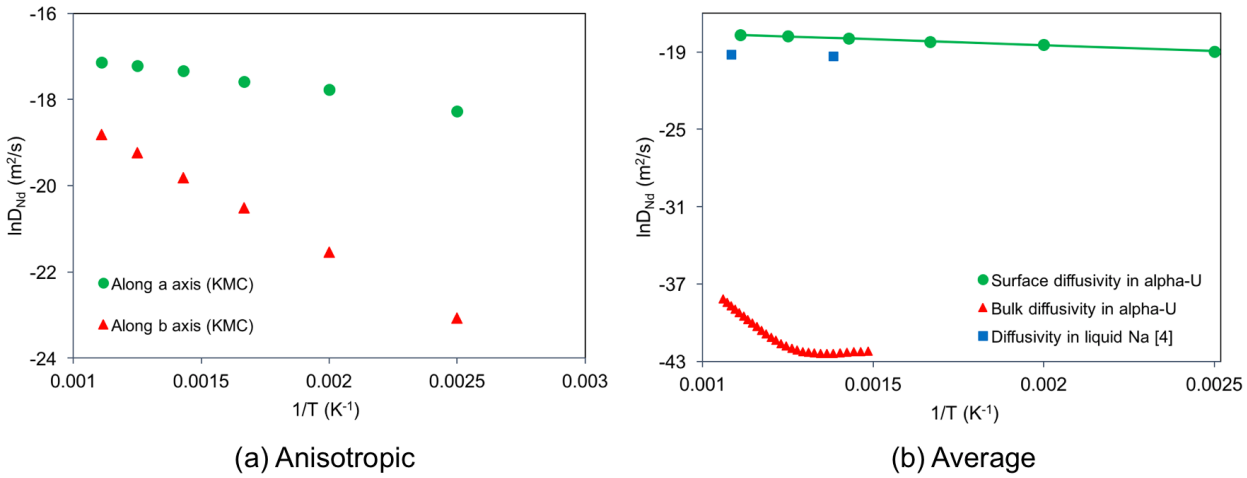

Fig. 11. (a) Arrhenius plot for anisotropic diffusivity of a Nd adatom along *a* and *b* axis on α-U (001) surface. (b) Arrhenius plot for average diffusivity of Nd adatom on α-U (001) surface. In our KMC simulations, Nd adatom diffusion is described as a series of hops between adjacent Hollow1 sites. The solid line represents the best fitting of KMC calculated surface diffusivity data using the Arrhenius equation.